Journal of Alloys and Compounds 893 (2022) 162030

Contents lists available at ScienceDirect

Journal of Alloys and Compounds

journal homepage: www.elsevier.com/locate/jalcom

Refractory TaTiNb, TaTiNbZr, and TaTiNbZrX (X = Mo, W) high entropy alloys by combined use of high energy ball milling and spark plasma sintering: Structural characterization, mechanical properties, electrical resistivity, and thermal conductivity

N.F. Shkodich[a,b,*], K.V. Kuskov[a], A.S. Sedegov[a], I.D. Kovalev[b], A.V. Panteleeva[a], Yu.S. Vergunova[b], Yu.B. Scheck[b], E. Panina[c], N. Stepanov[c], I. Serhiienko[d], D. Moskovskikh[a]

[a] Center of Functional Nanoceramics, National University of Science and Technology MISIS, Moscow 119049, Russia
[b] Merzhanov Institute of Structural Macrokinetics and Materials Science, Russian Academy of Sciences, Chernogolovka 142432, Russia
[c] Laboratory of Bulk Nanostructured Materials, Belgorod State University, Belgorod 308015 Russia
[d] Academic Research Center for Energy Efficiency, National University of Science and Technology MISIS, Moscow 119049, Russia

ARTICLE INFO

Article history:
Received 28 May 2021
Received in revised form 9 September 2021
Accepted 15 September 2021
Available online 20 September 2021

Keywords:
Refractory high entropy alloys
High energy ball milling
Spark plasma sintering
bcc solid solutions, electrical resistivity, thermal conductivity

ABSTRACT

Refractory TaTiNb, TaTiNbZr, and TaTiNbZrX (X = Mo, W) high entropy alloys were synthesized by combined use of high energy ball milling (HEBM) and spark plasma sintering (SPS). Powders of predominantly *bcc* TaTiNbZrX (X = Mo, W) refractory high entropy alloys (RHEAs) were successfully prepared by short-term HEBM (60 min) and then SPS-consolidated at 1373 K for 10 min. TEM analysis of the TaTiNbZrW HEA powder obtained after 60 min of HEBM revealed its nanocrystalline structure with an average grain size of up to 50 nm and predominantly uniform distribution of the elements on an atomic scale. The SPS consolidation at 1300°C led to an increase in grain sizes up to 100–300 nm. Thus prepared bulk RHEA materials showed ultra-high Vickers hardness of 8.5 GPa and 13 GPa for TaTiNbZrMo and TaTiNbZrW alloys, respectively. The room-temperature compressive strength of TaTiNbZrW RHEA alloy sintered from HEBM powders attained a value of 2665 MPa, which is 30% higher than that for the same alloy produced from non-milled powders. Bulk samples of synthesized RHEA show a higher electrical resistivity (r) compared to the samples prepared from non-milled powder blends. Within the temperature range 298–573 K, the maximum r value for TaTiNbZrW RHEA alloy was found to vary between 132 and 143.6 Ω cm. A decrease in thermal conductivity was observed: (a) upon introduction of Zr, Mo, and W atoms to TaTiNb-based alloys due to additional phonon scattering on lattice distortions caused by different radius and mass of Zr, Mo, and W atoms and (b) for the HEBM-prepared bulk alloys because of additional phonon scattering on the surface of mechanocomposites.

1. Introduction

Since the novel multi-component alloy design concept of high entropy alloys (HEAs) was suggested by J.W. Yeh in 2004 [1], it aroused increasing attention in the field of advanced metallic materials. The high mixing entropy of HEAs induced by an equiatomic or near-equiatomic configuration of five or more principal elements favors the formation of simple solid solution phases—face-centered cubic (*fcc*), body-centered cubic (*bcc*), hexagonal close-packed (*hcp*), or their combinations—rather than of intermetallic compounds [2,3]. Due to four core effects (high entropy, lattice distortion, sluggish diffusion, and cocktail effects) observed in HEAs [4], they can be tailored to possess outstanding chemical, mechanical and magnetic properties [5–10] for a variety of applications.

As is known, refractory metal-based alloys have always been used as the basis for the design of high-strength materials for high-temperature applications. HEAs based on refractory elements have attracted interest as promising materials for high-temperature applications since their first appearance in 2010 [6]. They have been proposed and characterized by Senkov et al. [6,11,12] who extended the HEA design concept to refractory alloys. It has been shown that the high-temperature strength of refractory high entropy alloys

* Corresponding author at: Center of Functional Nanoceramics, National University of Science and Technology MISIS, Moscow 119049, Russia.
E-mail address: n.f.shkodich@mail.ru (N.F. Shkodich).

https://doi.org/10.1016/j.jallcom.2021.162030
0925-8388/

Table 1
Calculated alloy parameters, *VEC*, Δr and $\Delta\chi$, for TaTiNb, TaTiNbZr, TaTiNbZrX (X = Mo, W) alloys.

Composition	ΔS_{mix}	VEC	Phase prediction	Δr, %	$\Delta\chi$
TaTiNb	1.31 R	4	*bcc*	5.3	0.027
TaTiNbZr	1.39 R	4.5	*bcc*	5.3	0.067
TaTiNbZrMo	1.61 R	4.8	*bcc*	5.9	0.17
TaTiNbZrW	1.61 R	4.8	*bcc*	5.8	0.21

(RHEAs) MoNbTaW and MoNbTaVW with a *bcc* structure at temperatures above 800 °C are significantly higher in comparison to conventional Ni-based superalloys [6]. Since then, more RHEAs—such as TiNbTaV, TiZrHfNbTa, MoVHfZrTi, Ti(V)WMoNbTa, and so on—with excellent mechanical strength at room and high temperatures had been designed [13–15].

Apart from composition, different synthesis routes were reported to yield a wide variety of microstructures [16]. To date, the most of reported RHEAs (95%) are being synthesized through the casting route [17]. However, casting of materials with high melting temperatures like RHEAs in industrial-relevant quantities can be associated with significant technical difficulties. Cast materials also usually contain inhomogeneities and casting defects (pores, etc) and have coarse microstructures [18]. Therefore, additional, often time- and cost-consuming, processing of the as-cast materials is usually required to use them for structural applications.

Another possible synthesis route is mechanical alloying (MA) which has been successfully applied to produce a variety of materials (intermetallics, ordered compounds, solid-solution alloys, nanocrystalline materials, RHEAs) with a refinement of grain size leading to improvement in mechanical properties and product homogeneity [17,19–22].

Recent reports in the field have shown that the RHEAs produced by combined use of MA and SPS display advantageous mechanical properties (especially in strength and ductility) as compared to the alloys fabricated by arc melting [17,23–25]. For instance, a WNbMoTaV RHEA with an average grain size of 5.3 μm and homogenous microstructures was fabricated by using MA and subsequent SPS consolidation [23]. The yield strength and plastic strain were found to grow from 1246 MPa to 2612 MPa, i.e. by 1.7% and 8.8%, respectively, as compared to the alloys with dendritic microstructure and coarse grains fabricated by arc melting.

Refractory CrMoNbTiW HEA synthesized [24] by mechanical alloying for 10 h followed by SPS consolidation has shown a high hardness (8.9 GPa) caused by the presence of residual the elements along with contaminations from milling bodies.

A drawback of conventional MA (long milling time, large amount of contaminants, low energy input) can be overcome by using short-term high energy ball milling (HEBM).

Recently [25], the technique of HEBM was successfully used to fabricate RHEAs from multicomponent powder mixtures for subsequent consolidation in the process of spark plasma sintering (SPS). This approach allows for the synthesis of multicomponent compounds at lower temperatures compared to melting points of starting refractory the elements.

However, there are still significant gaps in understanding the composition–processing, and structure–properties relationships in HEBM–SPS produced RHEAs. The TaTiNb and TaTiNbZr alloys prepared by usual casting route are known to have a dominating *bcc* structure and reasonable ductility [26,27]. The addition of Mo or W to TaTiNbZr cannot be expected to affect phase composition of the alloys [28], while cast TaTiNbZrMo alloy also have moderate ductility [29]. Meanwhile, the data on the mechanical behavior of TaTiNbZrW alloy are lacking in the literature.

Despite a large number of publications devoted to the synthesis and characterization of numerous RHEAs, the equiatomic TaTiNbZrMo and TaTiNbZrW alloys have been studied inadequately [30–32]. Primarily, the equiatomic and non-equiatomic TiNbTaZrMo high entropy alloys were proposed as promising biocompatible metallic materials [29]. In [28–30], this alloy with a structure of *bcc* solid solution (prepared by arc melting) has shown good strength, ductility, and biocompatibility close to that of pure Ti. The combination of induction melting, gas atomization, and selective laser melting (SLM) was used [31] to fabricate $Ti_{1.4}Nb_{0.6}Ta_{0.6}Zr_{1.4}Mo_{0.6}$ BioHEA powders and SLM-built parts (with a *bcc* structure) exhibiting low porosity, customizable shape, excellent yield stress, and good biocompatibility. Recently [32], the equiatomic TiZrNbMoTa alloyed powders with an *fcc* solid-solution structure were prepared by mechanical alloying (MA) for 30 h and then consolidated by spark plasma sintering (SPS) at 1300, 1400, 1500, and 1600 °C. The *bcc* phase and the ZrO_2 phase precipitated from the *fcc* solid solution during cooling down. RHEA with the highest compression fracture strength of 3759 MPa and fracture strain of 12.1% was obtained by SPS at 1400 °C. Surprisingly, the *fcc* structured HEA powders (rather than *bcc* structured ones) were obtained [32] during MA, according to the valence electron concentration (VEC) used as a criterion for phase formation in HEA. This can be explained by the formation of metal carbides with an *fcc* structure (e.g. TaC) during prolonged milling due to material contamination from carbide drum and balls.

To the best of our knowledge, the fabrication of TaTiNbZrMo and TaTiNbZrW RHEAs by combined use of short-term (60 min) HEBM and SPS consolidation has not been reported so far.

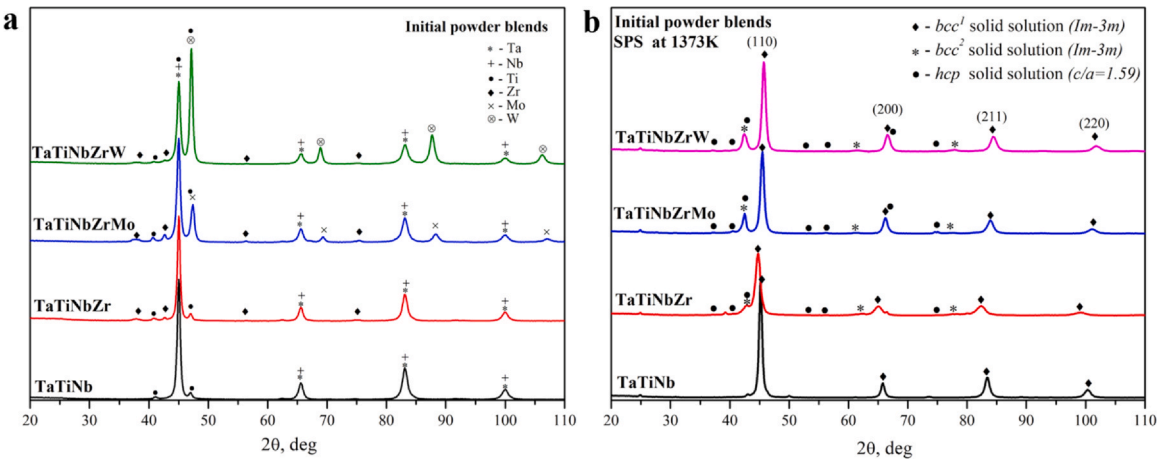

Fig. 1. XRD patterns of TaTiNb, TaTiNbZr, and TaTiNbZrX (X = Mo, W): (a) initial powder blends (indicated); (b) bulk samples derived from the powder mixtures (indicated) by SPS sintering at 1373 K. The spectra are shifted along the *y* axis for the sake of clarity.

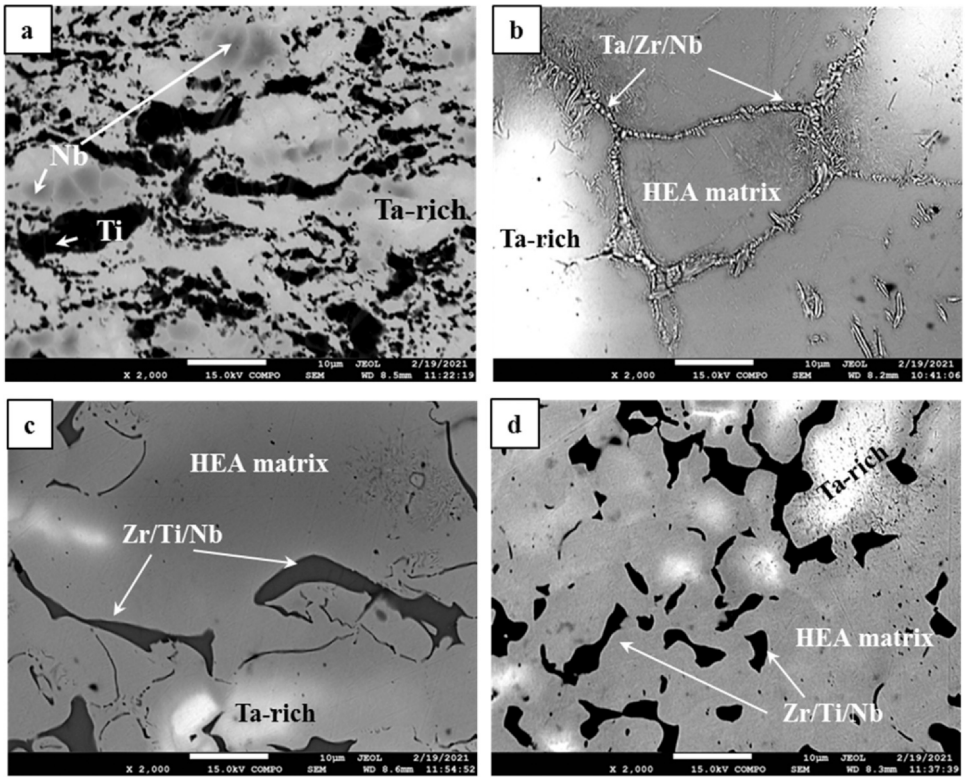

Fig. 2. SEM-BSE images for multicomponent alloys SPS consolidated at 1373 K: (a) TaTiNb, (b) TaTiNbZr, (c) TaTiZrNbMo, (d) TaTiZrNbW. Scale bar for all SEM images is 10 μm (2000×).

To get more systematic information, in this communication we report on a facile processing route for the fabrication of TaTiNb, TaTiNbZr, and TaTiNbZrX (X = Mo, W) RHEAs by combined use of short-term HEBM and SPS-consolidation to obtain bulk materials with enhanced mechanical properties, microhardness, electrical resistivity, and thermal conductivity at room and elevated temperatures. Note that the information on electrical resistivity or thermal conductivity of RHEAs is mostly lacking, although thermal conductivity is a significant characteristic of any high-temperature material. For the sake of comparison, the same alloys were fabricated by SPS consolidation from elemental powders (without HEBM).

2. Experimental

Commercial powders of Ta (99.9% pure, particle size 40–60 μm), Ti (99.2%, 40–60 μm), Nb (99.9%, 40–60 μm), Zr (99.6%, 100–200 μm), Mo (99.95%, 2–4.5 μm), W (99.98%, < 6 μm) were used as starting materials. Equiatomic amounts of the powders were mechanically treated in a water-cooled double-station planetary ball mill Activator-2S (Activator, Russia) using stainless steel cylindrical jars and balls (7 mm in diameter). In all cases the ball/powder weight ratio was 20: 1. The vial was evacuated and then filled with Ar at 4 atm to prevent the oxidation of powders during milling. Ball milling was run at rotation speeds of sun wheel/jars: 694/1388 rpm. Overall HEBM time (t) for all studied TaTiNb-based powder blends was 60 min (55 min in Ar and 5 min in C_2H_5OH).

Starting and milled TaTiNb, TaTiNbZr, and TaTiNbZrX (X = Mo, W) powders were SPS-consolidated in a vacuum in a Labox 650 facility (Sinter Land, Japan). The powder mixture was placed into a cylindrical graphite die (inner diameter 12.7 mm) and uniaxially compressed at 50 MPa and heated at a rate of 100 °C/min up to some preset sintering temperature at 1373 K by passing rectangular heavy-current current pulses through the sample. The dwell time at sintering temperature was 10 min. SPS-produced disks were 3–4 mm thick and 12.7 mm in diameter.

Starting, milled, and consolidated powders were characterized by XRD (DRON-4–07 diffractometer, Co-K_α radiation, 2θ = 20–110°), SEM (JEOL JSM-7600 F, Japan), and EDX (Oxford Inca spectrometer) using Aztec software. The microhardness of SPS-consolidated samples was measured in Vickers hardness tests with an Emco-Test DuraScan 70 (Austria) under applied load (4.9 N).

For TEM analysis, the lamellas of TaTiNbZrW HEA powder particle and HEA bulk sample were prepared using the focused ion beam technique (Nanolab 6000 Helios Dual SEM/FIB FEI, USA). Subtle structural studies and compositional analyses were performed using a Jeol JEM 2100 microscope (Japan) equipped with an Oxford X-Max 80 EDX detector (UK).

The thermal conductivity was calculated from the formula $\kappa = \lambda d C_p$, where λ is the thermal diffusivity as measured by laser flash method using an LFA 467 apparatus (Netzsch, Germany), C_p is the specific heat measured by a comparative method using LFA 467, and d is density. The electrical resistivity (r) was measured simultaneously on 1 × 3 × 12 mm^3 bars using a homemade electrical transport measuring system (Cryotel Ltd., Russia). The uncertainty of electrical resistivity measurements was within 8%, and that of the thermal conductivity was estimated to be within 5%, considering the uncertainties for λ and d.

Isothermal compression was carried out at 295 K and 873 K in the air using an Instron 300LX test machine equipped with a radial furnace. For high-temperature testing, specimens were put in the preheated furnace, which was kept at the desired temperature for ≈ 1 h, and held for 10 min before testing to equilibrate the temperature. The temperature of the specimen was controlled by a thermocouple attached to its side surface. The test specimen had a height of 6 mm and a diameter of 4 mm. The initial strain rate was 10^{-4} s^{-1}. Testing was carried out until specimen fracture or 50% strain.

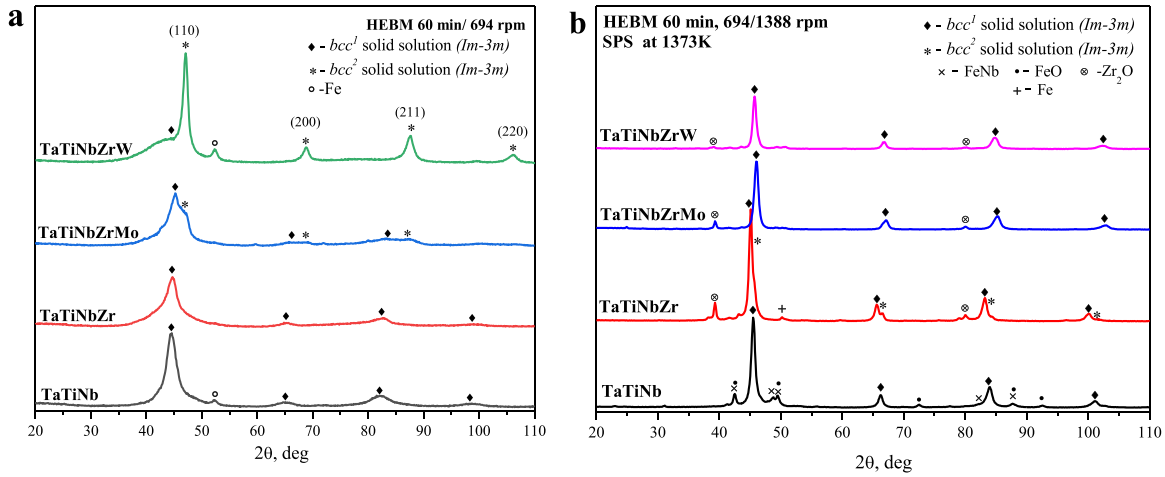

Fig. 3. XRD patterns of TaTiNb, TaTiNbZr, and TaTiNbZrX (X = Mo, W) powder blends: (a) milled by HEBM (60 min, 694/1388 rpm), (b) after HEBM followed by SPS at 1373 K. Compositions are indicated at the left. The spectra are shifted along the *y* axis for the sake of clarity.

Table 2
Crystallite size, lattice strain for HEBM TaTiNb, TaTiNbZr, and TaTiNbZrX (X = Mo, W) powder blends and SPS-consolidated samples.

		TaTiNb	TaTiNbZr	TaTiNbZrMo	TaTiNbZrW
		HEBM			
Crystallite size, nm	bcc^1	5	8	4	–
	bcc^2	–	–	6	10
Strain, %	bcc^1	0.91	1.35	0.46	–
	bcc^2	–	–	0.56	0.13
		HEBM+SPS			
Crystallite size, nm	bcc^1	34	21	–	
	bcc^2	–	27	20	44
Strain, %	bcc^1	0.38	0.18		–
	bcc^2		0.12	0.34	0.45

3. Results and discussion

For prediction of solid solution formation [3] in the studied alloys, alloy parameters—configurational entropy (ΔS_{config}) ≥ 1.61 *R* (universal gas constant), mixing enthalpy (ΔH_{mix}) within the range 11.6 kJ/mol < ΔH_{mix} < 3.2 kJ/mol, atomic size difference (δ) within the accepted limits 0 ≤ Δ*r* ≤ 8.5%, electronegativity ($\Delta\chi$) whose value should very small [33], and average valence electron concentration (VEC) (the *bcc* and *fcc* phases are formed for VEC < 6.87 and VEC ≥ 8.0, respectively; while *bcc* + *fcc* mixture coexist when 6.87 ≤ VEC ≤ 8.0)—were calculated and presented in Table 1.

For all studied compositions (see Table 1), the atomic size difference is well within the adopted limits 0 ≤ Δ*r* ≤ 6.5% for the solid solution formation; VEC < 6.87 falls into the range for the formation of a *bcc* solid solution [34]. The electronegativity (EN) difference for all TaTiNb, TaTiNbZr and TaTiNbZrX (X = Mo, W) alloys is in the range 0.027–0.21. As is known [35], electronegativity $\Delta\chi$ has little or no influence on the formation of a solid solution or amorphous phase. Even when no range has been prescribed for the formation of disordered solid solution, it was noted [33] that a larger value of $\Delta\chi$ is expected to aid the formation of a compound.

3.1. SPS of elemental powders

Fig. 1 presents the XRD patterns of ternary TaTiNb, quaternary TaTiNbZr, and multicomponent TaTiNbZrX (X = Mo, W) powder blends (Fig. 1a) and their alloys SPS-consolidated at 1373 K (Fig. 1b).

The initial powder blends exhibited expectedly strong and narrow Bragg peaks due to the crystalline structure of the constituent elements (Fig. 1a). The melting point of each principal element in studied compositions is much above 1373 K. The elemental powders did not reach complete metallurgical bonding during the sintering process.

The strong (110), (200), (211), (220) peaks—all from the phase with a *bcc* structure (*a* = 3.296 ± 0.002 Å)—were found in the XRD pattern of the ternary TaTiNb alloy. Two *bcc* phases with close lattice parameters (bcc^1, *a* = 3.478 ± 0.002 Å; and bcc^2, *a* = 3.328 ± 0.002 Å) and solid solution with *a hcp* structure were detected in quaternary TaTiNbZr. The addition of the fifth element, Mo or W, to TaTiNbZr alloy (all in equiatomic amounts) leads to the splitting of the main (110) XRD peak into bcc^1 and bcc^2 phases and an increase in the intensity of the latter. In case of the TaTiNbZrMo alloy, the bcc^1 and bcc^2 lattice parameters were calculated as *a* = 3.505 ± 0.002 Å and *a* = 3.327 ± 0.002 Å, respectively. For the TaTiNbZrW alloy, the respective magnitudes were *a* = 3.495 ± 0.001 Å and *a* = 3.261 ± 0.002 Å.

SPS-consolidated TaNiNb, TaTiNbZr, and TaTiNbZrX refractory alloys (X = Mo, W) represented a mixture of several phases (Fig. 2). The SEM-BSE data suggest that the light-gray primary islands correspond to the TaTiNb alloy enriched with Ta, while small gray inclusions and elongated grains can be related to Nb- and Ti-rich areas, respectively (Fig. 2a).

The SEM image of quaternary TaTiNbZr alloy (Fig. 2b) shows that it consists of a major gray matrix with thin intergranular regions and some amount of white/light gray domains. According to EDX results, the gray matrix corresponds to the solid solution with a homogeneous distribution of all the elements; whereas the intergranular regions are Ti-lean and have a laminar structure formed by bright Ta-rich layers and dark Zr-rich ones. Accordingly, *hcp* peaks can be assigned to (Zr, Nb)-based solid solution.

Fig. 2c shows the microstructure of refractory TaTiNbZrMo alloy. The gray color matrix corresponds to the HEA with the equiatomic concentration of the elements, while dark gray areas refer to TiNbZr-based solid solutions, the light-gray domains being Ta-enriched. A similar structure can be noticed in a refractory TaTiNbZrW alloy (Fig. 2d). Therefore, it can be deduced that complete dissolution of constituents had no time to occur in the course of sintering, and as a result, a complex microstructure formed by the nearly equiatomic solid solutions together with areas with elevated concentration of some certain the element is found.

3.2. Combined use of HEBM and SPS

The XRD pattern of TaTiNb, TaTiNbZr, and TaTiNbZrX (X = Mo, W) powder blends milled for 60 min are shown in Fig. 3a. XRD data of

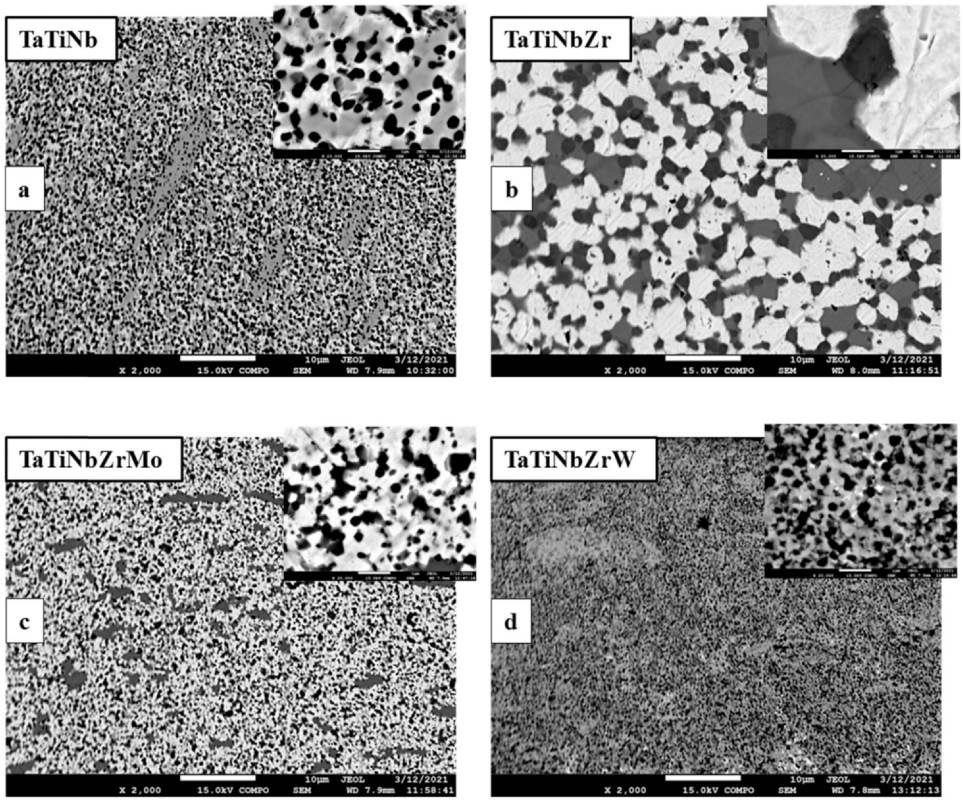

Fig. 4. SEM–BSE images of refractory alloys sintered by SPS from HEBM powders at 1373 K: (a) TaTiNb alloy, (b) TaTiNbZr alloy, (c) TaTiZrNbMo alloy, (d) TaTiZrNbW alloy. Magnification is 2000× for main SEM images (scale bar 10 μm) and 20,000× for inserts (scale bar 1 μm).

SPS-consolidated samples obtained from HEBM powder blends are presented in Fig. 3b.

During HEBM, the diffractions peaks of alloying elements broadened, decreased in their intensity, and partially overlapped. The formation of background around the (110), (200), (211), (220) *bcc* phase (a = 3.336 ± 0.002 Å) for ternary TaTiNb alloy was observed after 60 min of HEBM. Also, the diffraction (110) peak from Fe was detected by XRD. It is caused by the contamination with iron from steel drums and balls during the HEBM process.

For the TaTiNbZr powder blend after 60 min of HEBM, only a single *bcc* solid solution was observed. The absence of signal from Fe in the XRD spectra can be explained by its dissolution in the *bcc* TaTiNbZr phase of HEA powder.

The addition of Mo to TaTiNbZr powder blend leads to the splitting of the single *bcc* structured phase observed in TaTiNbZr HEA powder into two *bcc* solid solutions (bcc^1, a = 3.293 ± 0.003 Å; and bcc^2, a = 3.178 ± 0.002 Å). The bcc^2 phase corresponds to the pure Mo that had not dissolved TaTiNbZr solid solution during short-term HEBM.

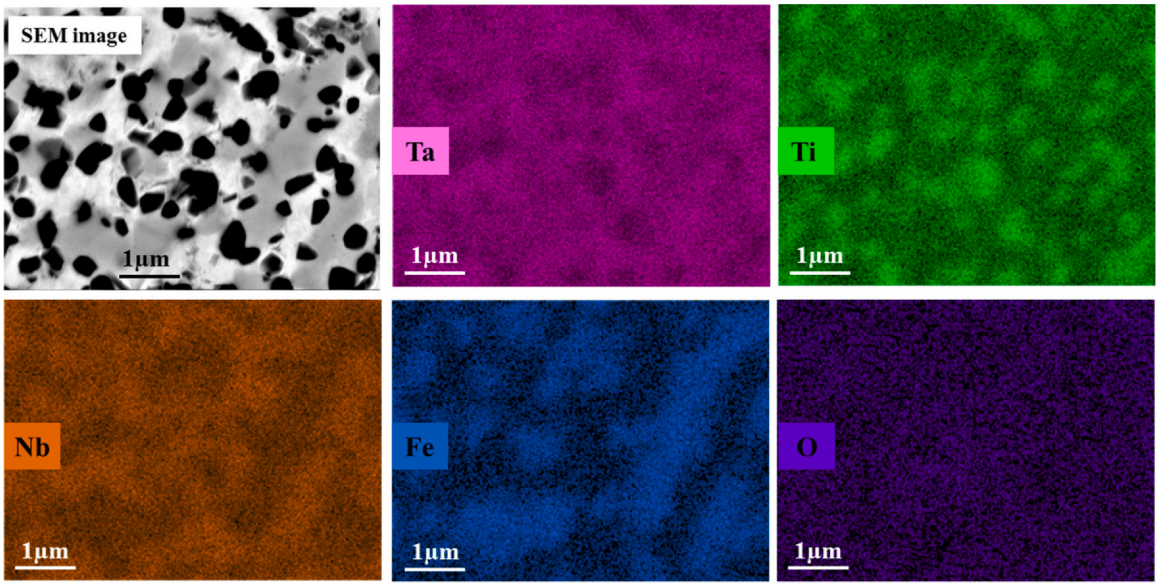

Fig. 5. SEM image and representative compositional EDX mapping obtained from the region of bulk TaTiNb RHEA (HEBM for t = 60 min, SPS at 1373 K).

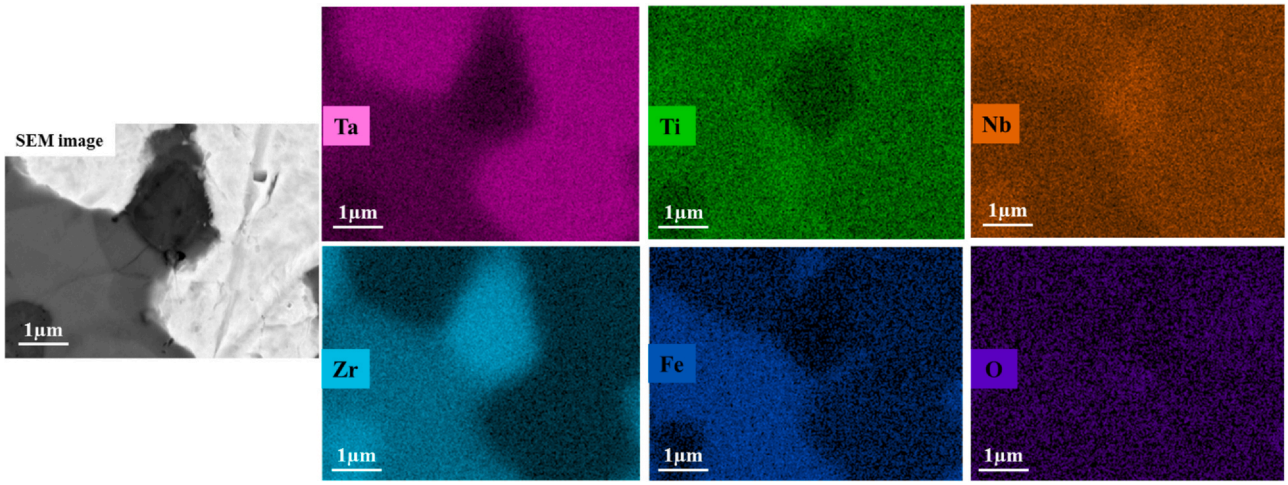

Fig. 6. SEM image and representative compositional EDX mapping obtained from the region of bulk TaTiNbZr RHEA (HEBM t = 60 min, SPS at 1373 K).

The TaTiNbZrW powder blend has shown similar structural changes during HEBM (60 min). Two phases with *bcc* structure were presented on XRD spectra: bcc^1 phase with very broad (110) peak corresponds to the solid solution based on all principal elements, the second one (bcc^2, a = 3.169 ± 0.002 Å) is likely pure W (*Im*-3*m*). During HEBM tungsten is partially dissolved in a multicomponent solid solution. In this case, the XRD peaks of pure Fe have not been detected.

The effect of HEBM on the crystallite size and strain in TaTiNb, TaTiNbZr, and TaTiNbZrX (X = Mo, W) powder blends and bulk samples were derived from line width analysis of XRD peaks. The pseudo-Voigt function as a convolution of a Gaussian and a Lorentzian component (the width of the Lorentzian component is related to the grain size, while the Gaussian width is related to the lattice strain of the sample) was used for fitting of the XRD peak profile and a Ge standard was used to correct instrumental broadening. Crystallite size, lattice strain for *bcc* phases were calculated for HEBM-processed samples using the Williams–Hall method [36]. For the bcc^1 phase in the TaTiNbZrW alloy adequate calculations were not possible due to the presence of a single broad (110) diffraction peak. The calculated results for HEBM powder blends and SPS-consolidated bulk samples are summarized in Table 2.

As follows from obtained results for all powder blends milled for 60 min at 694/1388 rpm, the HEBM leads to a decrease in the size of crystallites down to 4–10 nm depending on composition (see Table 2). In this case, lattice strains grew over this period up to 1.35%.

The SEM/EDX results for TaTiNb, TaTiNbZr, TaTiNbZrMo, and TaTiNbZrW RHEA powder particles milled for t = 60 min show that the elements are uniformly distributed on a micro-scale level (see in a supplementary file Figs. 1–4). The presence of 7–11 at% Fe (depending of composition) was detected.

As for SPS, an increase in the size of crystallites by a factor of 3–7 for SPS-consolidated samples (depending on their composition) was observed. However, the nanocrystalline nature of mechanically alloyed powders is retained after SPS at 1373 K due to special features of this process (synthesis is due to heating electric current pulses passing through the powder and a die, short holding time) (see Table 2). Also, it was observed that an increase in the number of the elements in alloy leads to a reduction of grain growth during SPS. The multi-elemental composition is likely to complicate the motion of atoms through the lattice due to different chemical environment and energy state at each site, thus making the diffusion sluggish [37,38]. The lattice strains are partially relieved during SPS (see Table 2).

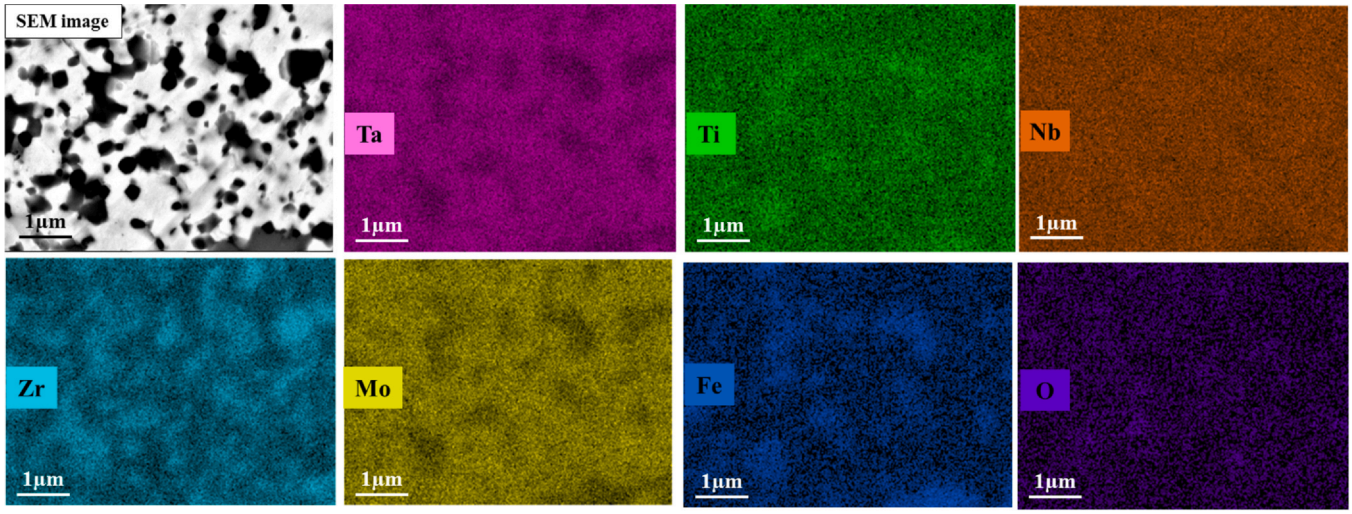

Fig. 7. SEM image and representative compositional EDX mapping result obtained from the region of bulk TaTiNbZrMo RHEA (HEBM for t = 60 min, SPS at 1373 K).

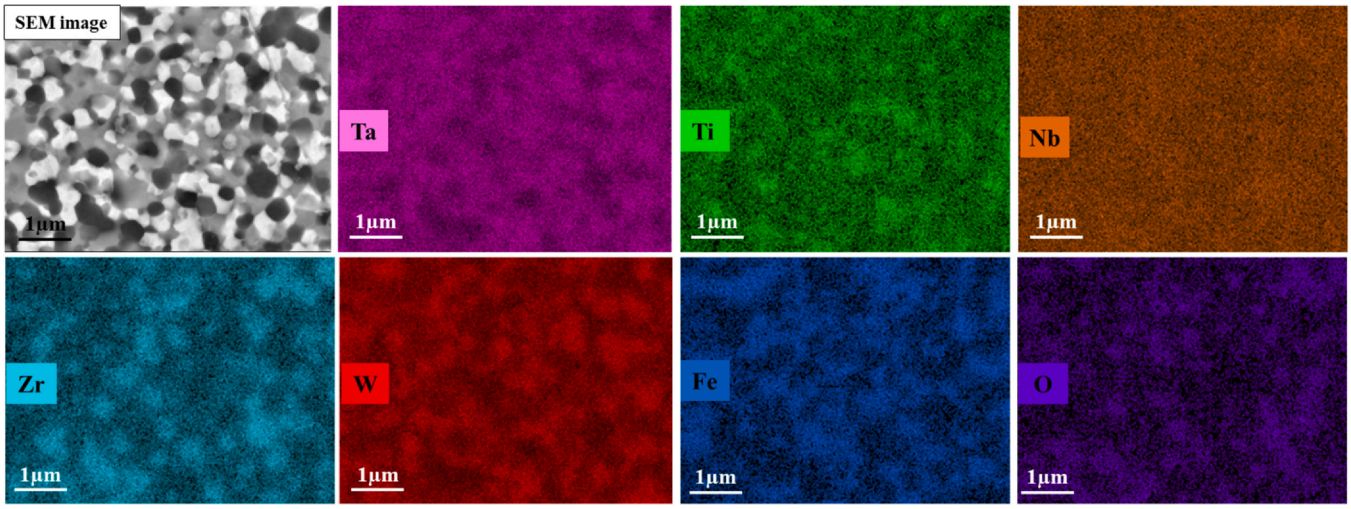

Fig. 8. SEM image and representative compositional EDX mapping result obtained from the region of bulk TaTiNbZrW RHEA (HEBM t = 60 min, SPS at 1373 K).

SEM–BSE micrographs of TaTiNb, TaTiNbZr, and TaTiNbZrX (X = Mo, W) SPS-consolidated samples from HEBM powders are presented in Fig. 4. All elements are seen to be more or less uniformly distributed throughout the material.

The chemical composition of the constituent phases was investigated by EDX/SEM. The results are presented in Figs. 5–8. In all HEBM-produced and SPS-consolidated samples, the presence of 7–11 at% Fe was detected. It is caused by friction grinding from the surface of milling bodies during HEBM. In our previous work [25], we have shown that the presence of Fe partitioned to the particles of the second phase (e.g. Zr_2Fe) can act as a strengthening agent improving mechanical properties of the resultant alloy.

A certain amount of oxygen is inevitably introduced after unloading from mill drums as well as during the sintering process.

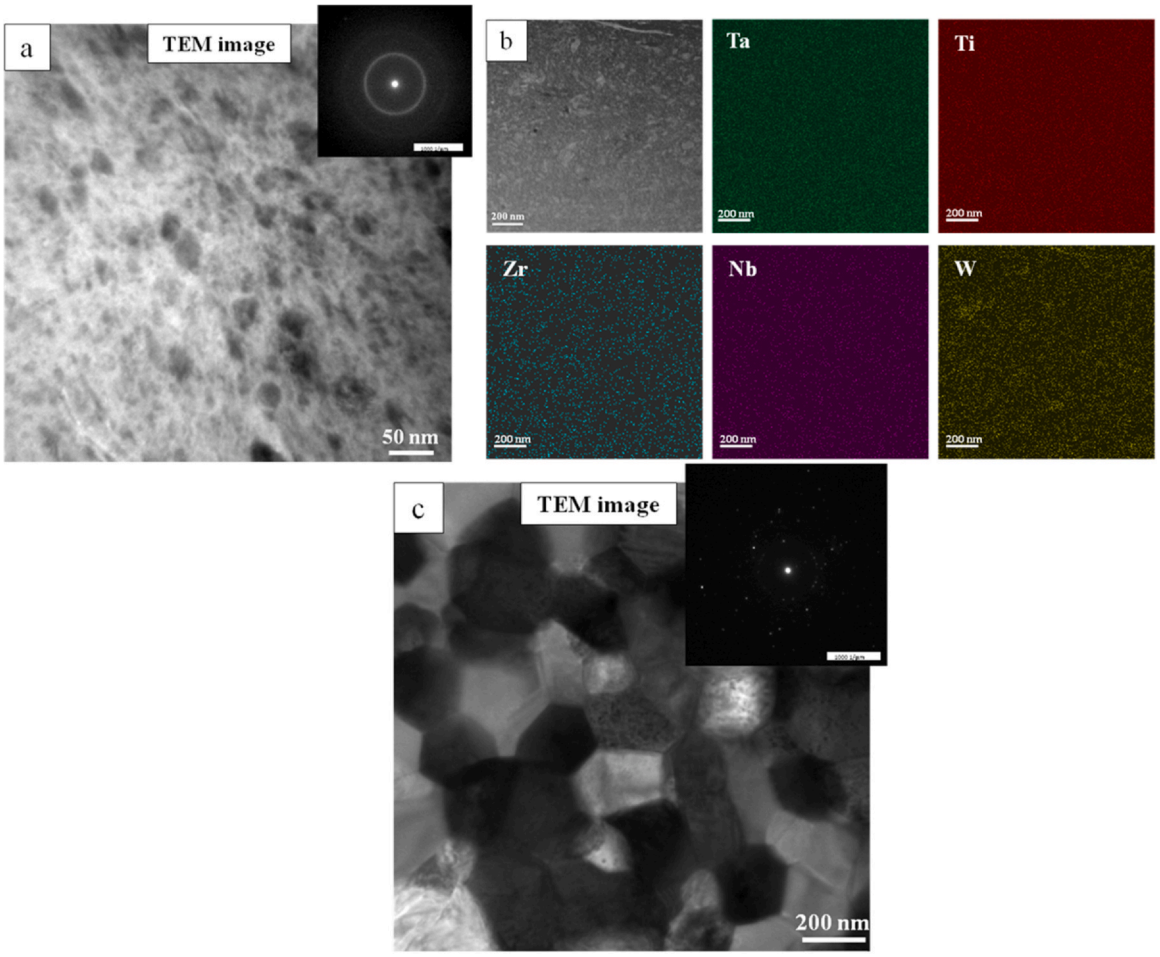

Fig. 9. (a) BF TEM image and selected area electron diffraction (SAED) pattern of 1 μm area and (b) STEM EDX mapping of TaTiNbZrW HEA powder produced after 60 min of HEBM, (c) BF TEM image and SAED pattern of 1 μm area of SPS-consolidated TaTiNbZrW HEA.

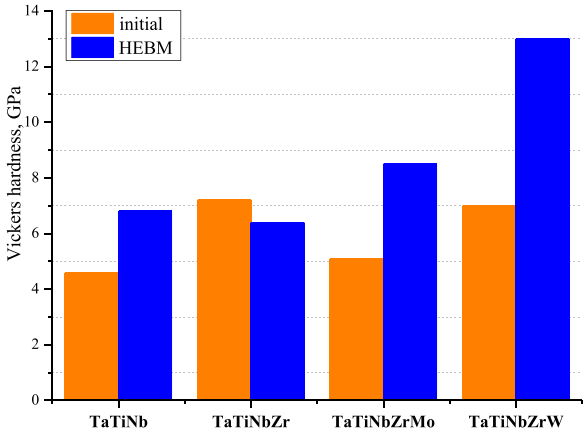

Fig. 10. Vickers hardness of SPS-consolidated samples (indicated) obtained from non-milled powder blends (orange bars) and HEBM powders (blue bar).

For the bulk TaTiNb refractory alloy, comparative analysis of SEM–BSE micrographs together with EDX results (Fig. 5) suggests that light-gray regions correspond to the TaTiNbFe-based solid solution enriched with Fe and Nb. Dark-gray areas with elongated morphology correspond to FeO-rich ones. Black domains on SEM-BSE can be related to Ti-rich regions. XRD results are in good agreement with SEM/EDX data.

The comparison between the microstructures (on a microscopic level) of bulk TaTiNbZr refractory alloy and other studied RHEAs showed that the grains in the former one are larger by a factor of 3–5. Based on EDX data (Fig. 6), medium-gray regions can correspond to ZrNb-rich *bcc* solid solutions while light gray areas, to *bcc* solid solution of pure of Zr and Fe, and dark-gray domains, to Zr/Nb/O-rich ones.

The SEM/EDX results for the bulk TaTiNbZrMo alloy (Fig. 7) show that white/light-gray areas represent a matrix with uniformly distributed principal elements. Dark-gray Fe/Zr/O-rich regions and black Zr-rich domains were also detected by EDX.

The bulk TaTiNbZrW RHEA exhibits a uniform ultrafine-grained microstructure composed of two *bcc* solid solutions: one is enriched with heavy the elements such as Ta, W, Nb (white domains on SEM/EDX maps), while others are Zr/Fe/Ti/O-rich regions (dark-gray), both are embedded in light-gray matrix with an approximately equal concentration of the elements (Fig. 8). Note that only one phase with a *bcc* structure was detected by XRD, apparently because of very small difference in lattice parameters of *bcc* solid solutions that cannot be discerned by conventional XRD analysis.

TEM analysis of the TaTiNbZrW HEA powder obtained after 60 min of HEBM revealed the formation of a nanocrystalline

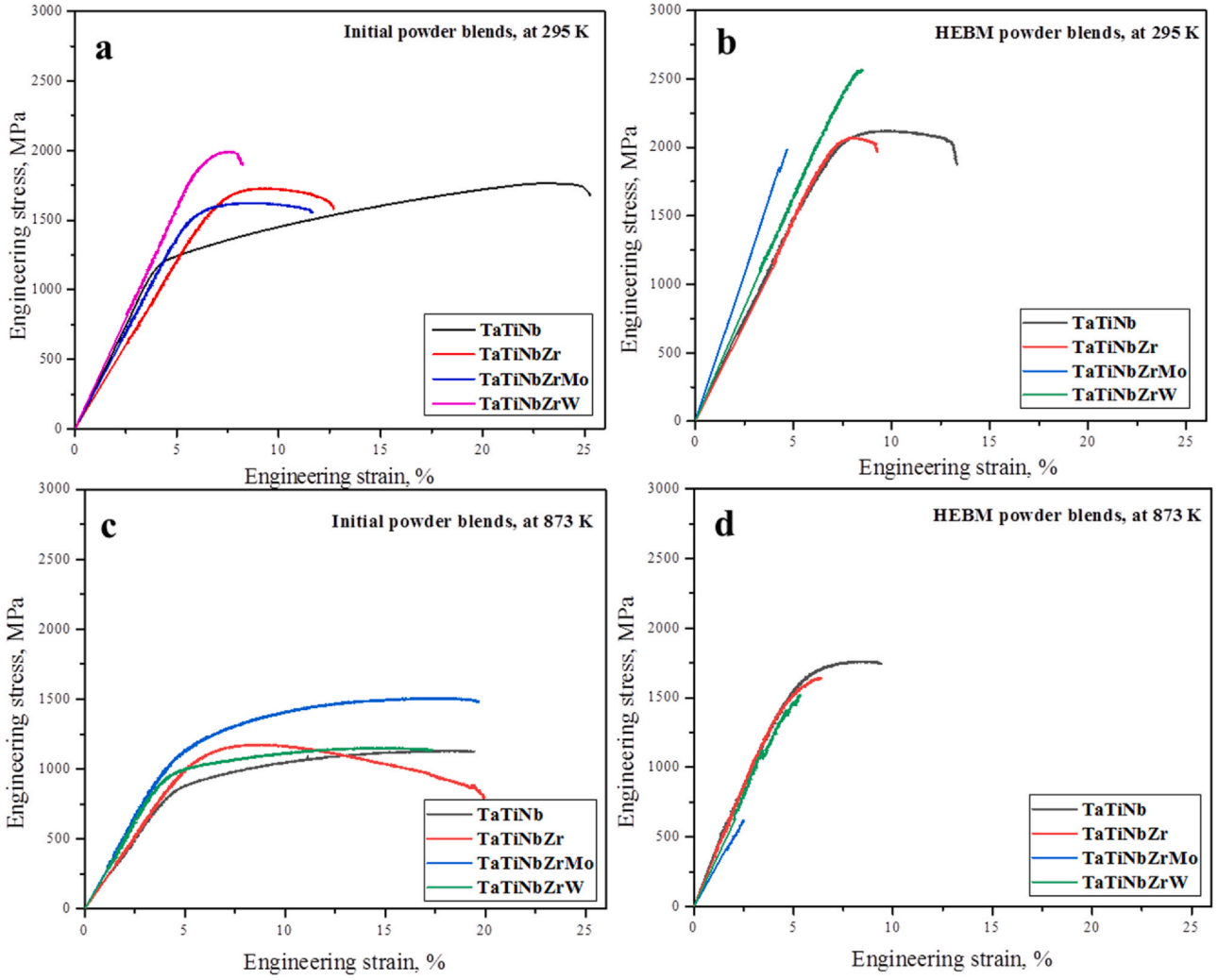

Fig. 11. Engineering compression stress–strain curves for samples SPS-consolidated from initial powder blends (a) at 295 K and (c) at 873 K; and for those SPS-consolidated from HEBM-processed powders (b) at 295 K and (d) at 873 K.

Table 3
Mechanical properties of TaTiNb, TaTiNbZr and TaTiNbZrX (X = Mo, W) alloys at 295 K and 873 K: yield stress σ_{YS}, compressive strength σ_{peak}, deformation ε, and Vickers microhardness $HV_{0.5}$.

Composition	Testing temperature, K	σ_{YS}, MPa	σ_{peak}, MPa	ε, %	$HV_{0.5}$, GPa
TaTiNb initial, SPS 1373 K	295	1135	1765	20	4.6 ± 0.3
	873	800	1130	14	–
TaTiNb HEBM, SPS 1373 K	295	1886	2120	6	6.8 ± 0.1
	873	1495	1762	4	–
TaTiNbZr initial, SPS 1373 K	295	1572	1728	6	7.2 ± 0.5
	873	1004	1178	16	–
TaTiNbZr HEBM, SPS 1373 K	295	1920	2070	3	6.4 ± 0.1
	873	1365	1642	2	–
TaTiNbZrMo initial, SPS 1373 K	295	1480	1625	6	5.1 ± 0.4
	873	1021	1509	14	–
TaTiNbZrMo HEBM, SPS 1373 K	295	–	1985	0	8.5 ± 0.1
	873	–	620	0	–
TaTiNbZrW initial, SPS 1373 K	295	1871	1992	2	(5.8–7.0) ± 0.1
	873	899	1155	13	–
TaTiNbZrW HEBM, SPS 1373 K	295	2458	2665	< 1	13.0 ± 0.1
	873	1387	1565	< 1	–

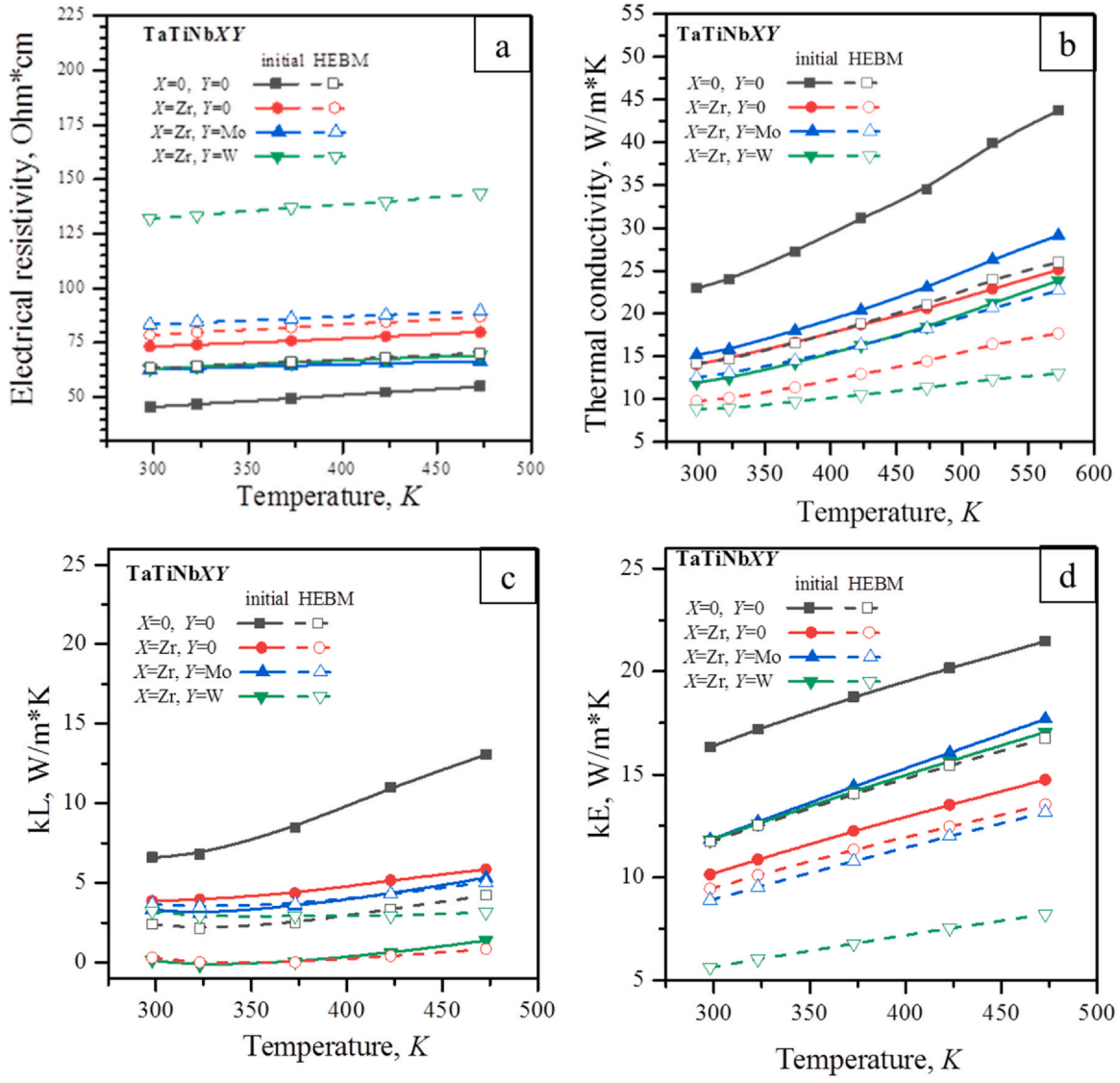

Fig. 12. (a) Electrical resistivity, (b) thermal conductivity, (c) lattice component of thermal conductivity, and (d) electron component of thermal conductivity, as a function of temperature for samples SPS-consolidated from starting powder blends and HEBM-processed powders. Compositions are indicated on the graph.

structure with an average particle size of up to 50 nm (Fig. 9a) and predominantly uniform distribution of the elements on an atomic scale (Fig. 9b). Phase analysis of the electron diffraction pattern (Fig. 9a, insert) showed the presence of reflections from the *bcc* phase, in agreement with the XRD data. The SPS consolidation of TaTiNbZrW HEA at 1300 ºC leads to an increase in grain sizes (Fig. 9c) up to 100–300 nm.

The microstructure of HEBM-produced alloys differs significantly from that prepared by sintering starting powder blends. Due to milling, we not only achieve uniform distribution of particles within mechanocomposites and get contaminated with Fe, O but also generate lattice defects. As a result, we observe the distribution of the elements over several solid solutions and/or the formation of oxides.

3.3. Mechanical properties

Mechanical properties of refractory TaTiNb, TaTiNbZr, and TaTiNbZrX (X = Mo, W) alloys at 295 K and 873 K—yield stress, σ_{YS}, peak stress, σ_{peak}, compressive strain to fracture, ε, and Vickers microhardness, $HV_{0.5}$—are presented at Figs. 10 and 11 and summarized in Table 3.

The results of H_v measurements are presented in Fig. 10. The hardness of TaTiNb alloy, TaTiNbZrMo, and TaTiNbZrW RHEAs prepared by HEBM (t = 60 min) and SPS consolidation (1373 K, τ = 10 min) exceed that for SPS-produced ones using unprocessed elemental powders by 50–80%. Moreover, the H_v value (13 GPa) for TaTiNbZrW RHEA (HEBM for 60 min, SPS at 1373 K) is the highest among the HEAs listed in [39]. An extraordinary high hardness of the alloy can be associated with (a) solid solution strengthening caused by strong lattice distortion [3] and (b) ultrafine-grained structure and associated grain boundary strengthening.

In case of TaTiNbZr RHEA, HEBM led to a 10-% drop in H_v, as compared to SPS-consolidated non-milled samples. This can be attributed to the phase/structural transformations taking place during HEBM. The high hardness of TaTiNbZr alloy obtained from starting powder blend can be explained by the presence of binary phase inclusions at HEA grain boundaries. The decrease in hardness of this alloy is caused by grain coarsening in the course of HEBM (Fig. 4).

The engineering compression stress–strain curves for TaTiNb, TaTiNbZr, and TaTiNbZrX (X = Mo, W) alloys obtained at 295 K and 873 K are shown in Fig. 11. For all studied alloys the compressive strength (at 295 K) of TaTiNbZrW RHEA alloy sintered from HEBM powders attained a maximum value of 2665 MPa (Fig. 11b), which is 30% higher than for the same alloy produced from non-milled powders (Fig. 11a).

At room temperature, the TaTiNb alloy produced from un-milled powders demonstrated relatively low yield stress (1135 MPa), good ductility (~20%), and fractured after reaching a stress of 1765 MPa, thus revealing reasonable strain hardening capacity (Fig. 11a). The refractory TaTiNbZr and TaTiNbZrMo exhibited a good combination of ductility and compression strength: 6% and ≈1500 MPa. The addition of W to TaTiNbZr alloy sharply decreased the ductility (down to 2–3%) but raised the strength (up to 1800 MPa)—due to the low ductility of pure W (about 1%) in comparison with a high one for Mo (10–15%) [40,41]. After HEBM, decent ductility (~6%) was only revealed by TaTiNb alloy. On the other hand, HEBM raised the compression strength by 20–30%, which can be associated with the grain refinement and generation of lattice defects.

The alloys produced in both routes, i.e. from elemental powders and after HEBM, demonstrated an increase (non-linear) in their strength with increasing number of components. Recently, a similar finding was reported for the Hf–Nb–Ta–Ti–Zr RHEAs produced by arc melting followed by thermomechanical processing [42]. In this case, an increase in material strength was attributed to higher solid solution hardening. It is reasonable to suggest that the same reason is applicable to variation in the strength of program alloys.

Here we have calculated the solid solution strengthening (SSS) for the hypothetical single-phase *bcc* alloys following the Coury–Kaufman–Clarke model [43]. For TaTiNb, TaTiNbZr, and TaTiNbZrX (X = Mo, W) alloys at room temperature, these magnitudes were found to have a value of 263, 1029, 1538, and 1594 MPa, respectively. The above values quantitatively correlate with the experimental data (Table 3). For example, the TaTiNb and TaTiNbZrW alloys have the lowest and the highest yield strength, respectively, in accordance with predicted SSS values. Yet the measured values of yield strength were noticeably higher than predicted by the SSS model. Several reasons are likely to be a reason. First, contrary to the single *bcc* phase structure assumed in the model, the real alloys have a complex multiphase structure (Figs. 1–8). The constitutive phases had different chemical compositions, often far from nominal ones. Therefore, the above calculations give only a rude assessment of SSS in the program alloys. Second, the alloys have a very fine structure with nanocrystalline grains (Table 2). Therefore, the Hall–Petch strengthening [44] must provide a significant contribution to the strength of the program alloys. However, due to a complex multiphase structure of the alloys, quantitative analysis of grain boundary strengthening looks problematic.

Typical strength–ductility trade-off is observed for the program alloys, i.e. stronger alloys exhibit lower ductility, probably due to lower strain hardening capacity. At 873 K, the ductility of the alloys produced from initial powders increased considerably (Fig. 11c) compared to that at 295 K (Fig. 11a), yet at the expense of their strength. For HEBM-produced alloys, the compression strength attained a value of 1600–1700 MPa (Fig. 11d). Interestingly, the ductility of the alloys at 873 K after HEBM decreased in comparison with that at room temperature. No solid explanation for this observation can be presented now. It can be supposed that due to a fine-grained structure, the oxygen in-take occurs in a very rapid mode at 873 K in the alloys produced by HEBM and cause significant embrittlement. However, additional work is required to verify this assumption.

3.4. Electrical resistivity and thermal conductivity

Temperature dependences of electrical resistivity for SPS-consolidated samples obtained from non-milled and HEBM-processed powder blends are presented in Fig. 12a. The resistivity (r) is seen to be metallic, i.e. it grows with increasing temperature.

An increase in r upon the implantation of Zr, Mo, and W atoms can be attributed to the electron scattering on structural defects. RHEA bulk samples produced from HEBM powders blends show higher r values compared to those derived from initials powder blends, which also be explained by a higher amount of structural defects. The addition of Mo and W atoms produces little or no influence on r, HEBM-produced bulk TaTiNbZrW alloy showing the largest magnitude. The latter can be due to a low density of sintered samples (85% of theoretical). The relative density of other samples was 95–97%.

Fig. 12b–d present thermal conductivity k and its components k_L and k_E as a function of temperature. Electronic component k_E was calculated in terms of the Wiedemann–Franz law. Introduction of Zr, Mo, and W atoms decreases k (Fig. 12b) due to additional phonon scattering on lattice distortions caused by different radius and mass of Zr, Mo, and W atoms [45]. Moreover, bulk RHEAs produced from HEBM powder blends show lower lattice component k_L (Fig. 12c) because of additional scattering on the surface of mechanocomposites. As concerning k_E (Fig. 12d), its decrease caused by the presence of Zr, Mo, and W atoms can be associated with lower mobility of charge carriers in the presence of guest atoms.

4. Conclusions

(1) Refractory TaTiNb, TaTiNbZr, TaTiNbZrX (X = Mo, W) high entropy alloys can be readily prepared by combined use of short-term high energy ball milling (HEBM) and spark plasma sintering (SPS).
(2) SPS consolidation of HEBM-produced RHEA powders at 1373 K for 10 min gives bulk RHEA materials with an ultra-high Vickers hardness of 8.5 GPa and 13 GPa for TaTiNbZrMo and TaTiNbZrW alloys, respectively.
(3) Nanocrystalline structures formed during HEBM of RHEA powders are preserved in SPS-consolidated refractory alloys.
(4) HEBM leads to an increase in compressive strength for all studied refractory alloys. At 295 K, the compressive strength of the TaTiNbZrW RHEA alloy sintered from HEBM-processed powders attained its maximum value at 2665 MPa, which is 30% higher than that of the same alloy produced from non-milled powders.
(5) HEBM-produced RHEA bulk samples show higher values of electrical resistivity (r) compared to those prepared from non-milled powders. A maximum electrical resistivity (132–143.6 Ω cm in the range 298–573 K) is exhibited by TaTiNbZrW RHEA.
(6) A decrease in thermal conductivity takes place: (a) upon introduction of Zr, Mo, and W atoms to TaTiNb-based alloys due to additional phonon scattering on lattice distortions caused by different radius and mass of Zr, Mo, and W atoms and (b) for the HEBM-prepared bulk alloys because of additional phonon scattering on the surface of mechanocomposites.

Credit Author Statement

N.F.Shkodich: Conceptualization, Methodology, Writing – original draft, Writing – review & editing. **K.V. Kuskov:** Methodology, Writing – review & editing. **A.S. Sedegov:** Methodology, Investigation. **I.D. Kovalev:** Methodology. **A.V. Panteleeva:** Methodology, Investigation. **Yu.S. Vergunova:** Investigation. **Yu.B. Scheck:** Writing – review & editing. **E. Panina:** Methodology, Validation. **N. Stepanov:** Writing – review & editing. **I. Serhiienko:** Writing – review & editing. **D.O. Moskovskikh:** Supervision, Writing – review & editing.

Declaration of Competing Interest

The authors declare that they have no known competing financial interests or personal relationships that could have appeared to influence the work reported in this paper.

Acknowledgments

This research was financially supported by the Russian Science Foundation (grant no. 18–79-10215). The authors gratefully thank Mr. Denis Klimenko from Belgorod State National Research University for his help with solid solution strengthening estimations. The work was carried out using the equipment of the Joint Research Center of Belgorod State National Research University "Technology and Materials".

Appendix A. Supporting information

Supplementary data associated with this article can be found in the online version at doi:10.1016/j.jallcom.2021.162030.

References

[1] J.W. Yeh, S.K. Chen, S.J. Lin, J.Y. Gan, T.S. Chin, T.T. Shun, C.H. Tsau, S.Y. Chang, Nanostructured high-entropy alloys with multiple principal elements: Novel alloy design concepts and outcomes, Adv. Eng. Mater. 6 (2004) 299–303, https://doi.org/10.1002/adem.200300567
[2] B. Cantor, I.T.H. Chang, P. Knight, A.J.B. Vincent, Microstructural development in equiatomic multicomponent alloys, Mater. Sci. Eng. A. (2004) 375–377, https://doi.org/10.1016/j.msea.2003.10.257
[3] D.B. Miracle, O.N. Senkov, A critical review of high entropy alloys and related concepts, Acta Mater. 122 (2017) 448–511, https://doi.org/10.1016/j.actamat.2016.08.081
[4] J.W. Yeh, Recent progress in high-entropy alloys, Ann. Chim. Sci. Mat. 31 (2006) 633–648, https://doi.org/10.3166/acsm.31.633-648
[5] P.K. Huang, J.W. Yeh, T.T. Shun, S.K. Chen, Multi-principal-element alloys with improved oxidation and wear resistance for thermal spray coating, Adv. Eng. Mater. 6 (2004) 74–78, https://doi.org/10.1002/adem.200300507
[6] O.N. Senkov, G.B. Wilks, D.B. Miracle, C.P. Chuang, P.K. Liaw, Refractory high-entropy alloys, Intermetallics 18 (2010) 1758–1765, https://doi.org/10.1016/j.intermet.2010.05.014
[7] C.Y. Hsu, J.W. Yeh, S.K. Chen, T.T. Shun, Wear resistance and high-temperature compression strength of Fcc CuCoNiCrAl0.5Fe alloy with boron addition, Metall. Mater. Trans. A Phys. Metall. Mater. Sci. 35 (A) (2004), https://doi.org/10.1007/s11661-004-0254-x
[8] P. Koželj, S. Vrtnik, A. Jelen, M. Krnel, D. Gačnik, G. Dražić, A. Meden, M. Wencka, D. Jezeršek, J. Leskovec, S. Maiti, W. Steurer, J. Dolinšek, Discovery of a FeCoNiPdCu high-entropy alloy with excellent magnetic softness, Adv. Eng. Mater. 21 (2019) 1801055, https://doi.org/10.1002/adem.201801055
[9] M.S. Lucas, L. Mauger, J.A. Muoz, Y. Xiao, A.O. Sheets, S.L. Semiatin, J. Horwath, Z. Turgut, Magnetic and vibrational properties of high-entropy alloys, J. Appl. Phys. 109 (2011) 07E307, https://doi.org/10.1063/1.3538936
[10] Y.J. Zhou, Y. Zhang, Y.L. Wang, G.L. Chen, Solid solution alloys of AlCoCrFeNi Tix with excellent room-temperature mechanical properties, Appl. Phys. Lett. 90 (2007) 181904, https://doi.org/10.1063/1.2734517
[11] O.N. Senkov, J.M. Scott, S.V. Senkova, F. Meisenkothen, D.B. Miracle, C.F. Woodward, Microstructure and elevated temperature properties of a refractory TaNbHfZrTi alloy, J. Mater. Sci. 47 (2012) 4062–4074, https://doi.org/10.1007/s10853-012-6260-2
[12] O.N. Senkov, J.M. Scott, S.V. Senkova, D.B. Miracle, C.F. Woodward, Microstructure and room temperature properties of a high-entropy TaNbHfZrTi alloy, J. Alloy. Compd. 509 (2011) 6043–6048, https://doi.org/10.1016/j.jallcom.2011.02.171
[13] R.J. Scales, D.E.J. Armstrong, A.J. Wilkinson, B.S. Li, On the brittle-to-ductile transition of the as-cast TiVNbTa refractory high-entropy alloy, Materialia 14 (2020) 100940, https://doi.org/10.1016/j.mtla.2020.100940
[14] Z.D. Han, N. Chen, S.F. Zhao, L.W. Fan, G.N. Yang, Y. Shao, K.F. Yao, Effect of Ti additions on mechanical properties of NbMoTaW and VNbMoTaW refractory high entropy alloys, Intermetallics 84 (2017) 153–157, https://doi.org/10.1016/j.intermet.2017.01.007
[15] O.N. Senkov, D.B. Miracle, K.J. Chaput, J.P. Couzinie, Development and exploration of refractory high entropy alloys - a review, J. Mater. Res. 33 (2018) 3092–3128, https://doi.org/10.1557/jmr.2018.153
[16] L. Raman, G. Karthick, K. Guruvidyathri, D. Fabijanic, S.V.S. Narayana Murty, B.S. Murty, R.S. Kottada, Influence of processing route on the alloying behavior, microstructural evolution and thermal stability of CrMoNbTiW refractory high-entropy alloy, J. Mater. Res. 35 (2020) 1556–1571, https://doi.org/10.1557/jmr.2020.128
[17] L. Raman, K. Guruvidyathri, G. Kumari, S.V.S. Narayana Murty, R.S. Kottada, B.S. Murty, Phase evolution of refractory high-entropy alloy CrMoNbTiW during mechanical alloying and spark plasma sintering, J. Mater. Res. 34 (2019) 756–766, https://doi.org/10.1557/jmr.2018.483
[18] D.G. Shaysultanov, N.D. Stepanov, A.V. Kuznetsov, G.A. Salishchev, O.N. Senkov, Phase composition and superplastic behavior of a wrought AlCoCrCuFeNi high-entropy alloy, JOM 65 (2013) 1815–1828, https://doi.org/10.1007/s11837-013-0754-5
[19] C.C. Koch, Nanocrystalline high-entropy alloys, J. Mater. Res. 32 (2017) 3435–3444, https://doi.org/10.1557/jmr.2017.341
[20] N.F. Shkodich, M. Spasova, M. Farle, D.Y. Kovalev, A.A. Nepapushev, K.V. Kuskov, Y.S. Vergunova, Y.B. Scheck, A.S. Rogachev, Structural evolution and magnetic properties of high-entropy CuCrFeTiNi alloys prepared by high-energy ball milling and spark plasma sintering, J. Alloy. Compd. 816 (2020) 152611, https://doi.org/10.1016/j.jallcom.2019.152611
[21] N.F. Shkodich, A.S. Rogachev, S.G. Vadchenko, D.O. Moskovskikh, N.V. Sachkova, S. Rouvimov, A.S. Mukasyan, Bulk Cu-Cr nanocomposites by high-energy ball milling and spark plasma sintering, J. Alloy. Compd. 617 (2014) 39–46, https://doi.org/10.1016/j.jallcom.2014.07.133
[22] D. Shaysultanov, A. Nepapushev, S. Zherebtsov, D. Moskovskikh, N. Stepanov, Structure and mechanical properties of a low-density AlCrFeTi medium entropy alloy produced by spark plasma sintering, Mater. Sci. Eng.: A 795 (2020) 140018, https://doi.org/10.1016/j.msea.2020.140018
[23] B. Kang, J. Lee, H.J. Ryu, S.H. Hong, Ultra-high strength WNbMoTaV high-entropy alloys with fine grain structure fabricated by powder metallurgical process, Mater. Sci. Eng.: A 712 (2018) 616–624, https://doi.org/10.1016/j.msea.2017.12.021
[24] N. Razumov, T. Makhmutov, A. Kim, B. Shemyakinsky, A. Shakhmatov, V. Popovich, A. Popovich, Refractory crmonbwv high-entropy alloy manufactured by mechanical alloying and spark plasma sintering: evolution of microstructure and properties, Materials 14 Basel,, 2021, https://doi.org/10.3390/ma14030621
[25] N. Shkodich, A. Sedegov, K. Kuskov, S. Busurin, Y. Scheck, S. Vadchenko, D. Moskovskikh, Refractory high-entropy hftatinbzr-based alloys by combined

use of ball milling and spark plasma sintering: effect of milling intensity, Metals 10 Basel,, 2020, https://doi.org/10.3390/met10091268
[26] J. Zýka, J. Málek, J. Veselý, F. Lukáč, J. Čížek, J. Kuriplach, O. Melikhova, Microstructure and room temperature mechanical properties of different 3 and 4 element medium entropy alloys from HfNbTaTiZr system, Entropy (Basel, Switz.) 21 (2019), https://doi.org/10.3390/e21020114
[27] O.N. Senkov, J. Gild, T.M. Butler, Microstructure, mechanical properties and oxidation behavior of NbTaTi and NbTaZr refractory alloys, J. Alloy. Compd. 862 (2021) 158003, https://doi.org/10.1016/j.jallcom.2020.158003
[28] T. Nagase, K. Mizuuchi, T. Nakano, Solidification microstructures of the ingots obtained by arc melting and cold crucible levitation melting in TiNbTaZr medium-, Entropy (Basel, Switz.) 21 (2019), https://doi.org/10.3390/e21050483
[29] M. Todai, T. Nagase, T. Hori, A. Matsugaki, A. Sekita, T. Nakano, Novel TiNbTaZrMo high-entropy alloys for metallic biomaterials, Scr. Mater. 129 (2017) 65–68, https://doi.org/10.1016/j.scriptamat.2016.10.028
[30] T. Hori, T. Nagase, M. Todai, A. Matsugaki, T. Nakano, Development of non-equiatomic Ti-Nb-Ta-Zr-Mo high-entropy alloys for metallic biomaterials, Scr. Mater. 172 (2019) 83–87, https://doi.org/10.1016/j.scriptamat.2019.07.011
[31] T. Ishimoto, R. Ozasa, K. Nakano, M. Weinmann, C. Schnitter, M. Stenzel, A. Matsugaki, T. Nagase, T. Matsuzaka, M. Todai, H.S. Kim, T. Nakano, Development of TiNbTaZrMo bio-high entropy alloy (BioHEA) super-solid solution by selective laser melting, and its improved mechanical property and biocompatibility, Scr. Mater. 194 (2021) 113658, https://doi.org/10.1016/j.scriptamat.2020.113658
[32] C. Zhu, Z. Li, C. Hong, P. Dai, J. Chen, Microstructure and mechanical properties of the TiZrNbMoTa refractory high-entropy alloy produced by mechanical alloying and spark plasma sintering, Int. J. Refract. Met. Hard Mater. 93 (2020) 105357, https://doi.org/10.1016/j.ijrmhm.2020.105357
[33] A.K. Singh, A. Subramaniam, On the formation of disordered solid solutions in multi-component alloys, J. Alloy. Compd. 587 (2014) 113–119, https://doi.org/10.1016/j.jallcom.2013.10.133
[34] S. Guo, C. Ng, J. Lu, C.T. Liu, Effect of valence electron concentration on stability of fcc or bcc phase in high entropy alloys, J. Appl. Phys. (2011), https://doi.org/10.1063/1.3587228
[35] S. Guo, C.T. Liu, Phase stability in high entropy alloys: formation of solid-solution phase or amorphous phase, Prog. Nat. Sci.: Mater. Int. 21 (2011) 433–446, https://doi.org/10.1016/S1002-0071(12)60080-X
[36] G.K. Williamson, W.H. Hall, X-ray line broadening from filed aluminium and wolfram, Acta Metall. 1 (1953) 22–31, https://doi.org/10.1016/0001-6160(53)90006-6
[37] M.H. Tsai, J.W. Yeh, High-entropy alloys: a critical review, Mater. Res. Lett. 2 (2014) 107–123, https://doi.org/10.1080/21663831.2014.912690
[38] K.Y. Tsai, M.H. Tsai, J.W. Yeh, Sluggish diffusion in Co-Cr-Fe-Mn-Ni high-entropy alloys, Acta Mater. 61 (2013) 4887–4897, https://doi.org/10.1016/j.actamat.2013.04.058
[39] S. Gorsse, M.H. Nguyen, O.N. Senkov, D.B. Miracle, Database on the mechanical properties of high entropy alloys and complex concentrated alloys, Data Br. 21 (2018), https://doi.org/10.1016/j.dib.2018.11.111
[40] C. Ren, Z.Z. Fang, M. Koopman, B. Butler, J. Paramore, S. Middlemas, Methods for improving ductility of tungsten - A review, Int. J. Refract. Met. Hard Mater. 75 (2018) 170–183, https://doi.org/10.1016/j.ijrmhm.2018.04.012
[41] G. Liu, G.J. Zhang, F. Jiang, X.D. Ding, Y.J. Sun, J. Sun, E. Ma, Nanostructured high-strength molybdenum alloys with unprecedented tensile ductility, Nat. Mater. 12 (2013) 344–350, https://doi.org/10.1038/nmat3544
[42] R.R. Eleti, N. Stepanov, N. Yurchenko, D. Klimenko, S. Zherebtsov, Plastic deformation of solid-solution strengthened Hf-Nb-Ta-Ti-Zr body-centered cubic medium/high-entropy alloys, Scr. Mater. 200 (2021) 113927, https://doi.org/10.1016/j.scriptamat.2021.113927
[43] F.G. Coury, M. Kaufman, A.J. Clarke, Solid-solution strengthening in refractory high entropy alloys, Acta Mater. 175 (2019) 66–81, https://doi.org/10.1016/j.actamat.2019.06.006
[44] Z.C. Cordero, B.E. Knight, C.A. Schuh, Six decades of the Hall–Petch effect – a survey of grain-size strengthening studies on pure metals, Int. Mater. Rev. 61 (2016) 495–512, https://doi.org/10.1080/09506608.2016.1191808
[45] F. Körmann, Y. Ikeda, B. Grabowski, M.H.F. Sluiter, Phonon broadening in high entropy alloys, Npj Comput. Mater. 3 (2017) 36, https://doi.org/10.1038/s41524-017-0037-8